



Shell-cluster transition in  $^{48}\text{Ti}$ M. Okada <sup>1</sup>, W. Horiuchi <sup>1,2,3,4,\*</sup> and N. Itagaki <sup>1,2,3,†</sup><sup>1</sup>*Department of Physics, Osaka Metropolitan University, Osaka 558-8585, Japan*<sup>2</sup>*Nambu Yoichiro Institute of Theoretical and Experimental Physics (NITEP), Osaka Metropolitan University, Osaka 558-8585, Japan*<sup>3</sup>*RIKEN Nishina Center, Wako 351-0198, Japan*<sup>4</sup>*Department of Physics, Hokkaido University, Sapporo 060-0810, Japan*

(Received 28 February 2024; accepted 2 May 2024; published 24 May 2024)

**Background:** The existence of  $\alpha$  ( $^4\text{He}$  nucleus) clustering in the medium-mass region of nuclear systems is a fundamental and intriguing question. However, the recent analysis of the  $\alpha$  knockout reaction on  $^{48}\text{Ti}$  [*Phys. Rev. C* **103**, L031305 (2021)] poses a puzzle: The microscopic wave function gives an  $\alpha$  knockout cross section that is two orders of magnitude smaller than the experiment, while basic nuclear properties such as the charge radius and the electromagnetic transition probabilities are well explained.

**Purpose:** The ground-state structure of  $^{48}\text{Ti}$  is investigated by using proton- and  $\alpha$ -nucleus elastic scattering at a few to several hundred MeV, which offers different sensitivity to the region of the nuclear density profiles.

**Method:** Four types of density distributions, the  $jj$ -coupling shell model and three cluster model configurations, are generated in a single scheme by the antisymmetrized quasicluster model (AQCM). The angular distribution of the proton- and  $\alpha$ - $^{48}\text{Ti}$  elastic scattering cross sections are obtained with a reliable high-energy reaction theory, the Glauber model.

**Results:** The  $jj$ -coupling shell model configuration is found to best reproduce the proton-nucleus elastic scattering cross section. On the other hand, the trace of the  $\alpha$  cluster structure in the tail region of the wave function is embedded in the  $\alpha$ -nucleus elastic scattering cross section.

**Conclusions:** Our results suggest that the structure of the nucleus changes as a function of distance from the center, from the  $jj$ -coupling shell model structure in the surface region to the  $\alpha+^{44}\text{Ca}$  cluster structure in the tail region. This picture is consistent with the finding of the  $\alpha$  knockout reaction on  $^{48}\text{Ti}$ .

DOI: [10.1103/PhysRevC.109.054324](https://doi.org/10.1103/PhysRevC.109.054324)

## I. INTRODUCTION

It is well known that  $\alpha$  clustering plays a crucial role in light nuclei. In addition to the light-mass region, the existence of  $\alpha$  clustering in the medium-mass region is a fundamental and intriguing question. However, the degree of the clustering is expected to be smaller because the effect of the spin-orbit interaction, which acts to break up the  $\alpha$  clusters near the nuclear surface and induces the independent nucleon motion of the  $jj$  coupling shell model, becomes stronger with increasing mass number, more precisely with increasing total angular momentum  $j$  of single particles [1]. A possible candidate for a medium-heavy nucleus with the cluster structure is  $^{44}\text{Ti}$ , which is a  $Z = N$  nucleus. The presence of an  $\alpha + ^{40}\text{Ca}$  structure was predicted in Ref. [2], and subsequently the inversion doublet structure was experimentally confirmed [3,4], providing supporting evidence for the presence of an asymmetric cluster structure. However, the general persistence of the  $\alpha$  cluster structure in the Ti isotopes, including the  $\beta$  stable ones with more neutrons in the  $pf$  shell, requires further discussion.

In this respect, the recent analysis of the  $\alpha$  knockout reaction on  $^{48}\text{Ti}$  poses a vexing puzzle. It is presumed that  $^{48}\text{Ti}$  has less  $\alpha$  cluster components compared to  $^{44}\text{Ti}$  and  $^{52}\text{Ti}$  [5]; nevertheless, the  $\alpha$  particle is knocked out with a certain cross section. However, the wave function obtained with the structure calculation based on the antisymmetrized molecular dynamics (AMD) exhibits the dominance of the mean-field type and gives an  $\alpha$  knockout reaction cross section that is two orders of magnitude smaller than the experimental one [6]. The cross section can indeed be explained if the presence of an  $\alpha + ^{44}\text{Ca}$  cluster structure is assumed with a huge relative distance of about 4.5 fm but other fundamental properties of  $^{48}\text{Ti}$  such as the charge radius and the electromagnetic transition probabilities cannot be explained with this cluster wave function.

With the aim of providing some insight into this question, we study the ground state of  $^{48}\text{Ti}$ . In fact, the cross section of the  $\alpha$  knockout reaction is only sensitive to the  $\alpha$  clustering in the tail region of the wave function. This is because the information about the more inner region of the wave function is drowned out by the strong  $\alpha$  absorption. The transition matrix density shows that the  $\alpha$  knockout reaction tells us nothing about the character of the wave function within a radius of 5 fm [6]. Therefore, even if the more inner part of the wave function is different from a simple

\*whoriuchi@omu.ac.jp

†itagaki@omu.ac.jp

$\alpha$  cluster structure, it does not affect the  $\alpha$  knockout cross section.

In this paper, we use a proton and an  $\alpha$  particle to probe the ground state properties of  $^{48}\text{Ti}$ . Medium- to high-energy elastic scattering is useful to study the nuclear density profiles, enabling one to distinguish whether  $^{48}\text{Ti}$  is  $\alpha$  cluster-like or  $jj$ -coupling shell-like. Here, the wave functions for both the shell and cluster configurations are consistently produced in a single scheme, which is achieved by using the antisymmetrized quasicluster model (AQCM) [7–20]. This model allows us to smoothly transform the cluster model wave function into the  $jj$ -coupling shell model wave function, and we can treat the two on the same footing. The analyses of the proton-nucleus elastic scattering for the ground states of  $^{44}\text{Ti}$  and  $^{52}\text{Ti}$  were already carried out by combining AQCM and the Glauber model [21], showing significant difference in the cross sections, especially around the first diffraction peak. Unfortunately, no experimental result for  $^{44}\text{Ti}$  and  $^{52}\text{Ti}$  is available. In the present case of  $^{48}\text{Ti}$ , which is a  $\beta$ -stable Ti isotope, there are experimental data to be compared. Similar studies of the distinction between the cluster and shell densities have been carried out for light nuclei such as  $^{12}\text{C}$ ,  $^{16}\text{O}$  [22], and  $^{20}\text{Ne}$  [23].

The paper is organized as follows. Section II summarizes the formulation of the present approach. We briefly explain how to calculate the density distributions for shell and cluster configurations using the AQCM and the elastic scattering cross section with a high-energy reaction theory, the Glauber model. Our results are presented in Sec. III. We discuss the relationship between density profiles of the model wave functions and observables such as the proton- and  $\alpha$ -nucleus elastic scattering cross sections. Finally, the conclusion is given in Sec. IV.

## II. METHODS

### A. Shell model type and cluster model type wave functions based on AQCM

Based on AQCM, we introduce shell model type (S-type) and cluster model type (C-type) wave functions. In both cases, the single-particle wave function has a Gaussian shape as in the Brink model [24],

$$\phi_i = \left(\frac{2\nu}{\pi}\right)^{3/4} \exp[-\nu(\mathbf{r}_i - \boldsymbol{\zeta}_i)^2] \chi_i \eta_i, \quad (1)$$

where  $\chi_i$  and  $\eta_i$  are the spin and the isospin parts of the wave function, respectively. The parameter  $\nu$  is a size parameter, and  $\boldsymbol{\zeta}_i$  is the Gaussian center parameter. The total wave function  $\Phi$  is the antisymmetrized product of these single-particle wave functions,

$$\Phi = \mathcal{A} \left\{ \prod_{i=1}^A \phi_i \right\}, \quad (2)$$

where  $\mathcal{A}$  is the antisymmetrizer and  $A = 48$  is the mass number.

These 48 single-particle wave functions consist of a  $^{40}\text{Ca}$  core and eight valence nucleons. The  $^{40}\text{Ca}$  core can be described as ten  $\alpha$  clusters with small relative distances, which

is consistent with the shell model description of  $^{40}\text{Ca}$  due to the antisymmetrization effect. Each  $\alpha$  cluster is defined as four nucleons (proton spin-up, proton spin-down, neutron spin-up, neutron spin-down) sharing a common value for the Gaussian center parameter  $\boldsymbol{\zeta}_i$ . The actual positions of the ten  $\alpha$  clusters for the  $^{40}\text{Ca}$  core are described in Ref. [12].

For the eight valence nucleons, we first introduce three  $\alpha$  clusters ( $^{12}\text{C}$ ) around the  $^{40}\text{Ca}$  core and then remove four protons afterwards. These three  $\alpha$  clusters are introduced to have an equilateral triangular shape with a small relative distance around the  $^{40}\text{Ca}$  core. The spin parts of the single particles in the three  $\alpha$  clusters are also introduced with the equilateral triangular symmetry as described in Ref. [12]. These single-particle orbits in the three  $\alpha$  clusters are excited to the  $pf$  shell due to the antisymmetrization effect with the nucleons in the  $^{40}\text{Ca}$  core. However, there is no spin-orbit contribution yet unless the  $\alpha$  clusters are broken. Therefore, next, these single-particle orbits are transformed into the  $f_{7/2}$  orbits of the  $jj$ -coupling shell model by giving the imaginary parts to the Gaussian center parameters based on the transformation of AQCM [11],

$$\boldsymbol{\zeta}_i = \mathbf{R}_i + i\Lambda \mathbf{e}_i^{\text{spin}} \times \mathbf{R}_i. \quad (3)$$

Here  $\mathbf{R}_i$  represents the spatial location of the  $i$ th single particle, and  $\mathbf{e}_i^{\text{spin}}$  is a unit vector for the intrinsic spin. The imaginary parts of the Gaussian center parameters represent imparted momenta to the nucleons, and  $\alpha$  clusters are broken in such a way that spin-up and spin-down nucleons are boosted in opposite directions and perform time-reversal motions. The parameter  $\Lambda$  controls the breaking of the  $\alpha$  clusters, and the  $^{48}\text{Ti}$  wave function is constructed by removing four protons from the twelve nucleons around the  $^{40}\text{Ca}$  core.

For the shell model wave function, S-type, to break clusters, the  $\Lambda$  value is set to 1 for all the eight nucleons. In this way, the  $jj$ -coupling shell model wave function of  $^{48}\text{Ti}$  [ $(f_{7/2})^2$  for the protons and  $(f_{7/2})^6$  for the neutrons around the  $^{40}\text{Ca}$  core] is generated.

Next, we introduce the cluster model wave function, C-type. For the four nucleons (proton spin-up, proton spin-down, neutron spin-up, neutron spin-down) in the  $f_{7/2}$  orbits around the  $^{40}\text{Ca}$  core, we set  $\Lambda = 0$  in Eq. (3) and remove the imaginary part of the Gaussian center parameters; they are returned to an  $\alpha$  cluster. This  $\alpha$  cluster is separated from the rest ( $^{44}\text{Ca}$ ) by the distance of  $d$  fm. After setting all these Gaussian center parameters of S-type and C-type, the whole system is moved to satisfy the condition of  $\sum_{i=1}^{48} \langle \mathbf{r}_i \rangle = 0$ .

Once the model wave function  $\Phi$  is set, the intrinsic density distribution  $\tilde{\rho}_t(\mathbf{r})$  is obtained by calculating the expectation value of  $\sum_{i \in t} \delta(\mathbf{r}_i - \mathbf{r})$ ,

$$\tilde{\rho}_t(\mathbf{r}) = \langle \Phi | \sum_{i \in t} \delta(\mathbf{r}_i - \mathbf{r}) | \Phi \rangle / \langle \Phi | \Phi \rangle, \quad (4)$$

where the summation is taken over protons ( $t = p$ ) or neutrons ( $t = n$ ). The center-of-mass wave function can be eliminated by using a Fourier transform [25] as

$$\int d\mathbf{r} e^{i\mathbf{k}\cdot\mathbf{r}} \rho_t^{\text{int}}(\mathbf{r}) = \exp\left(\frac{k^2}{8A\nu}\right) \int d\mathbf{r} e^{i\mathbf{k}\cdot\mathbf{r}} \tilde{\rho}_t(\mathbf{r}), \quad (5)$$

and we use  $\rho_i^{\text{int}}(\mathbf{r})$  as the intrinsic density free of center of mass motion. The density distribution in the laboratory frame is finally obtained by averaging the intrinsic density distribution over the angles [26] as

$$\rho_i(r) = \frac{1}{4\pi} \int d\hat{\mathbf{r}} \rho_i^{\text{int}}(\mathbf{r}). \quad (6)$$

### B. Elastic scattering cross section within the Glauber model

Proton-nucleus elastic scattering is one of the most direct ways of obtaining information on the density profile. We remark that the full density distribution can be obtained by measurements up to backward angles [27,28]. As long as the nuclear surface density is of interest, only the cross sections at the forward angles, i.e., the cross section at the first peak in the proton-nucleus diffraction is needed to extract the ‘‘diffuseness’’ of the density distribution as prescribed in Ref. [29]. To relate the density profile to the reaction observables we employ a high-energy microscopic reaction theory, the Glauber model [30].

The differential cross section of the elastic scattering is given by

$$\frac{d\sigma}{d\Omega} = |f(\theta)|^2 \quad (7)$$

with the scattering amplitude of the nucleus-nucleus elastic scattering [31]

$$f(\theta) = F_C(\theta) + \frac{ik}{2\pi} \int d\mathbf{b} e^{-iq \cdot \mathbf{b} + 2i\eta \ln(kb)} (1 - e^{i\chi_{xT}(\mathbf{b})}), \quad (8)$$

where  $F_C(\theta)$  is the Rutherford scattering amplitude,  $\mathbf{b}$  is the impact parameter vector, and  $\eta$  is the Sommerfeld parameter. As the nuclear scattering occurs in several hundred MeV, relativistic kinematics is used for the wave number  $k$ .

Here, we treat proton- or  $\alpha$ -target nucleus ( $xT$ ,  $x = p$  or  $\alpha$ ;  $T = \text{target nucleus}$ ) system. The optical phase shift function  $\chi_{xT}$  contains all the dynamical information for the  $xT$  system within the Glauber model, but its evaluation involves multiple integration. For practical calculations, the optical limit approximation (OLA) [30,31] is used to compute the optical phase shift function as

$$i\chi_{pT}(\mathbf{b}) \approx - \int d\mathbf{r} [\rho_p(\mathbf{r})\Gamma_{pp}(\mathbf{b} - \mathbf{s}) + \rho_n(\mathbf{r})\Gamma_{pn}(\mathbf{b} - \mathbf{s})], \quad (9)$$

for a proton-nucleus system, where a single-particle coordinate is expressed by  $\mathbf{r} = (s, z)$  with  $z$  being the beam direction. Further, we evaluate the optical phase shift function for an  $\alpha$ -nucleus system with

$$\begin{aligned} i\chi_{\alpha T}(\mathbf{b}) \approx & - \int \int d\mathbf{r} d\mathbf{r}' [\rho_p^\alpha(\mathbf{r}')\rho_p(\mathbf{r})\Gamma_{pp}(\mathbf{b} + \mathbf{s}' - \mathbf{s}) \\ & + \rho_p^\alpha(\mathbf{r}')\rho_n(\mathbf{r})\Gamma_{pn}(\mathbf{b} + \mathbf{s}' - \mathbf{s}) \\ & + \rho_n^\alpha(\mathbf{r}')\rho_p(\mathbf{r})\Gamma_{np}(\mathbf{b} + \mathbf{s}' - \mathbf{s}) \\ & + \rho_n^\alpha(\mathbf{r}')\rho_n(\mathbf{r})\Gamma_{nn}(\mathbf{b} + \mathbf{s}' - \mathbf{s})], \end{aligned} \quad (10)$$

where  $\rho^\alpha$  is the intrinsic density distribution of the  $\alpha$  particle with the  $(0s)^4$  harmonic oscillator configuration and a

size parameter reproducing the measured charge radius. The parametrization of the proton-proton (neutron-proton) profile function  $\Gamma_{pp} = \Gamma_{nn}$  ( $\Gamma_{pn} = \Gamma_{np}$ ) is given in Ref. [32]. Once the above inputs are set, the theory has no tunable parameter, and so the resulting reaction observables are a direct reflection of the density profiles of the target nucleus. This model works well as shown, for example, in Refs. [33,34], and its accuracy compared to those obtained by the full evaluation of the optical phase shift function was discussed in Refs. [34–37].

## III. RESULTS AND DISCUSSIONS

### A. Properties of the wave functions

Here we generate the shell-model-like (S-type) and cluster-model-like (C-type) configurations and show their properties. The C-type is further subdivided into C-type-1, C-type-2, and C-type-3 depending on the size parameter  $\nu$  in Eq. (1) and the  $\alpha$ - $^{44}\text{Ca}$  distance  $d$ . All these configurations reproduce the experimental charge radius of  $^{48}\text{Ti}$  [38].

#### 1. Shell-model-like configuration (S-type)

As shown in Table I, the shell-model-like configuration (S-type) has a total harmonic oscillator quanta  $\langle N \rangle$  of 84.0. This means that eight nucleons with  $N = 3$  are located outside the  $^{40}\text{Ca}$  core with  $N = 60$ . Given the  $\Lambda$  value of 1 in Eq. (3) for the eight nucleons around  $^{40}\text{Ca}$ , the  $jj$ -coupling shell model state is realized, with two protons and six neutrons occupying the  $f_{7/2}$  orbits. This is confirmed by the calculation of the expectation values of the one-body spin-orbit operator  $\sum_{i=1}^{48} \mathbf{l}_i \cdot \mathbf{s}_i$ , which is listed in the  $\langle LS \rangle$  column, where  $\mathbf{l}_i$  and  $\mathbf{s}_i$  stand for the orbital angular momentum and spin operators of the  $i$ th nucleon, respectively. Here, there is no contribution from the  $^{40}\text{Ca}$  core part, and one nucleon in the  $f_{7/2}$  orbit has the  $\mathbf{l} \cdot \mathbf{s}$  value of  $1.5\hbar^2$ , and thus,  $1.5\hbar^2 \times 8 = 12\hbar^2$  is the ideal value of the  $jj$ -coupling shell model. We can confirm that our model reproduces this ideal value. The size parameter  $\nu$  of the single particle wave functions in Eq. (1) is chosen to be  $0.1269 \text{ fm}^{-2}$ , which reproduces the root-mean-square (rms) radius of the point protons (column  $r_p$ ) derived as 3.50 fm. The rms radii of the point neutrons ( $r_n$ ) and matter distribution ( $r_m$ ) are obtained as 3.61 and 3.56 fm, respectively.

#### 2. $\alpha$ -cluster-like configuration (C-type)

The  $\alpha$ -cluster-like configuration (C-type) has the structure of  $^{44}\text{Ca}$  plus  $\alpha$ . This can be obtained by setting  $\Lambda = 0$  for the two protons and two neutrons around  $^{44}\text{Ca}$ . These four nucleons form an  $\alpha$  cluster. Furthermore, the center of this  $\alpha$  cluster can be separated from  $^{44}\text{Ca}$  with the  $jj$ -coupling shell model configuration by the distance of  $d$  fm.

We prepare three  $\alpha$ -cluster-like configurations (C-type-1, C-type-2, and C-type-3). They have different  $\nu$  and  $d$  values but all three configurations reproduce the experimentally observed  $r_p$ .

For C-type-1, the size parameter  $\nu$  ( $0.1267 \text{ fm}^{-2}$ ) is set so as to reproduce  $r_p$  of the subsystem,  $^{44}\text{Ca}$ , 3.42 fm. Meanwhile, the parameter  $d$  for the relative distance between  $^{44}\text{Ca}$  and  $^4\text{He}$  is determined to reproduce  $r_p$  of the whole system,  $^{48}\text{Ti}$ , 3.50 fm. As shown in Table I, the  $d$  parameter must

TABLE I. Properties of the shell-model-like (S-type) and  $\alpha$ -cluster-model-like (C-type-1, C-type-2, and C-type-3) configurations for  $^{48}\text{Ti}$ . See text for details. The experimental point-proton rms radius ( $r_p$ ) of  $^{48}\text{Ti}$  is 3.50 fm extracted from Ref. [38].

	$\nu$ (fm $^{-2}$ )	$d$ (fm)	$\langle N \rangle$	$\langle LS \rangle$ ( $\hbar^2$ )	$r_p$ (fm)	$r_n$ (fm)	$r_m$ (fm)	$a_p$ (fm)	$a_n$ (fm)	$a_m$ (fm)
S-type	0.1269		84.0	12.0	3.50	3.61	3.56	0.544	0.531	0.536
C-type-1	0.1267	0.1	84.0	5.98	3.50	3.62	3.56	0.596	0.577	0.586
C-type-2	0.1299	2.379	84.6	5.99	3.50	3.61	3.56	0.611	0.585	0.599
C-type-3	0.1395	4.5	87.4	6.00	3.50	3.58	3.54	0.636	0.603	0.620

be very small in this case, and the resulting configuration is almost like a zero distance limit between  $^{44}\text{Ca}$  and  $^4\text{He}$ .

For C-type-2, the size parameter  $\nu$  (0.1299 fm $^{-2}$ ) is set so as to reproduce  $r_p$  of  $^{40}\text{Ca}$ , 3.38 fm. Again, the parameter  $d$  for the relative distance between  $^{44}\text{Ca}$  and  $\alpha$  is determined to reproduce  $r_p$  of the whole system,  $^{48}\text{Ti}$ , and, in this case, the finite value of  $d = 2.379$  fm is obtained.

For C-type-3, we mimic the wave function that reproduces the  $\alpha$  knockout reaction cross section. As mentioned above, the  $\alpha$  knockout reaction is reproduced by the cluster wave function with the  $\alpha$ - $^{44}\text{Ca}$  distance of 4.5 fm [6]. Therefore, here we set  $d = 4.5$  fm. To reproduce  $r_p$  of  $^{48}\text{Ti}$ ,  $\nu = 0.1395$  fm $^{-2}$  is required.

As shown in Table I, the harmonic oscillator quanta  $\langle N \rangle$  increases with the value of  $d$ ; the  $\langle N \rangle$  value of 84.0 is obtained for C-type-1 ( $d = 0.1$  fm), which increase to 84.6 for C-type-2 ( $d = 2.379$  fm) and 87.4 for C-type-3 ( $d = 4.5$  fm). For the expectation values of the one-body spin-orbit operator,  $\langle LS \rangle$ , since the  $^{40}\text{Ca}$  core and  $\alpha$  cluster parts do not contribute, the value comes only from the four neutrons around  $^{40}\text{Ca}$ . The ideal value is  $6\hbar^2$ ; a neutron in  $f_{7/2}$  has a contribution of  $1.5\hbar^2$ , and the actual values are close to it, as shown in the column  $\langle LS \rangle$ .

## B. Density distributions

Figures 1(a) and 1(b) show the point-proton and point-neutron density distributions of  $^{48}\text{Ti}$ , respectively, as a function of  $r$ , the distance from the origin. Despite the fact that all these density distributions give the same charge radii, they have different density profiles. In the following subsection, we will discuss the proton- $^{48}\text{Ti}$  elastic scattering, which is sensitive to the density in the region that the value is about

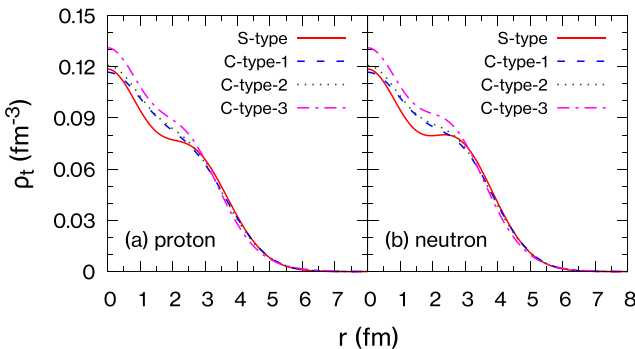


FIG. 1. Density distributions of  $^{48}\text{Ti}$  for (a) point protons and (b) point neutrons as a function of  $r$ , the distance from the origin.

half of the central one. This half-density region corresponds to  $r \approx 3$  fm, which we call the surface region. Meanwhile, the  $\alpha$  knockout reaction is sensitive to the wave function  $r \gtrsim 5$  fm [6], which can be called the tail region. To quantify the density profiles around the half-density region, it is convenient to evaluate the nuclear diffuseness for proton ( $a_p$ ), neutron ( $a_n$ ), and matter ( $a_m$ ) density distributions [29] by minimizing

$$\int_0^\infty dr r^2 |\rho_t(r) - \rho_t^{2\text{pF}}(r)| \quad (11)$$

with

$$\rho_t^{2\text{pF}}(r) = \frac{\rho_0}{1 + \exp\left(\frac{r-R_t}{a_t}\right)}. \quad (12)$$

Table I lists those calculated diffuseness values. The S-type configuration exhibits the smallest diffuseness values, i.e., the sharpest nuclear surface, and the nuclear surface becomes more diffused as the  $\alpha$ - $^{44}\text{Ca}$  cluster structure develops. As we will see later, differences in these diffuseness values are actually reflected in the elastic scattering cross sections.

The difference in the density distributions becomes more visible when  $r^{2n}$  ( $n$  integer) is multiplied. Figure 2 shows the

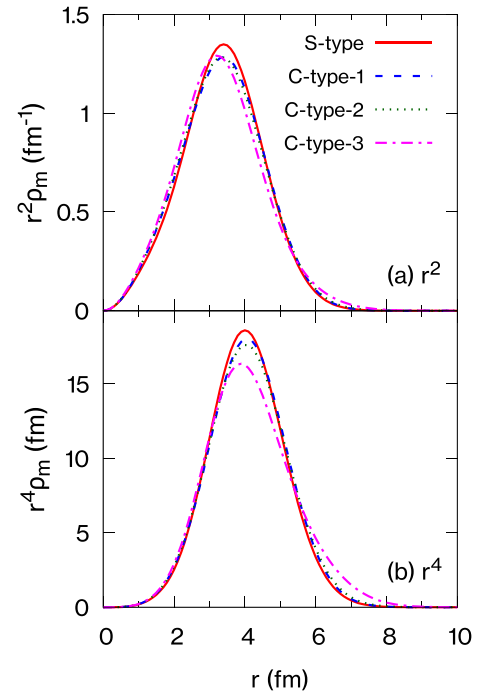


FIG. 2. Matter density distributions of  $^{48}\text{Ti}$  ( $\rho_m$ ) multiplied by (a)  $r^2$  and (b)  $r^4$  as a function of the distance from the origin,  $r$ .

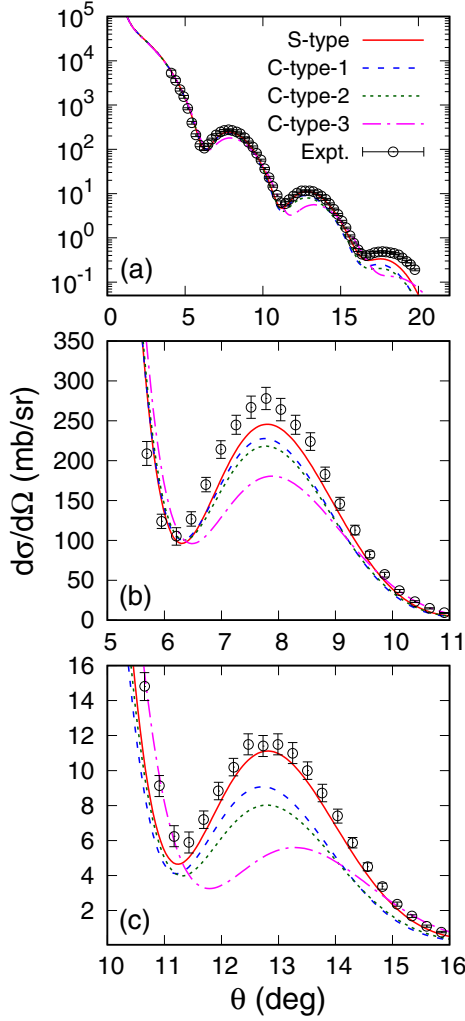


FIG. 3. Differential cross sections for the proton- $^{48}\text{Ti}$  elastic scattering at the incident energy of 1000 MeV in logarithmic (a) and linear (b), (c) scales as a function of the scattering angle. See text for details. The experimental data (incident energy of 1044 MeV) are taken from Ref. [39].

matter density distributions of  $^{48}\text{Ti}$  ( $\rho_m$ ) multiplied by (a)  $r^2$  and (b)  $r^4$ . The integration of  $4\pi r^2 \rho_m$  over  $r$  gives the particle number, and thus, in Fig. 2(a), the four areas that the four lines create together with the horizontal axis are equal. We see some differences beyond the half-density radius,  $r \gtrsim 3$  fm in the  $r^2 \rho_m$  distribution. In Fig. 2(b), the distribution of C-type-3 is significantly shifted to the larger  $r$  side compared to the other three lines. This characteristic feature of C-type-3 shown in the  $r^4 \rho_m$  distribution stems from its large clustering, which affects the  $\alpha$ -nucleus elastic scattering cross section at the first diffraction peak, where the signature of the large  $\alpha$  clustering is embedded, as we will discuss later.

### C. Proton- $^{48}\text{Ti}$ and $\alpha$ - $^{48}\text{Ti}$ elastic scattering

These differences between the density distributions are reflected in the diffraction patterns of the proton-nucleus elastic scattering. Figure 3 shows the differential cross section for the proton- $^{48}\text{Ti}$  elastic scattering. The proton incident energy

is chosen to be 1000 MeV, and the experimental data (incident energy of 1044 MeV) are taken from Ref. [39]. Three of the four nuclear densities, except for C-type-3, are in reasonable agreement with the experimental result up to the second peak [Fig. 3(a)], but for a more accurate comparison, we plot the cross sections in a linear scale in Figs. 3(b) and 3(c). The angle and height of the first peak position reflect the size and diffuseness of the target nucleus, and Fig. 3(b) shows the experimental data around this region is best reproduced by the S-type configuration. This means that the  $^{48}\text{Ti}$  nucleus has a density distribution close to the  $jj$ -coupling shell model picture around its surface region. Figure 3(c) shows the cross sections around the second peak, and the agreement between the experimental data and the result of S-type becomes even better than for the first peak region. It should be noted that in the present S-type configuration, the valence two protons and six neutrons occupy the  $f_{7/2}$  orbits. In reality, the nucleon interaction may induce the particle-hole excitation and the mixing of the  $p_{3/2}$  orbits. In this case, the occupation of the  $p_{3/2}$  orbits diffuses the nuclear surface [40] and plays a role of reducing the cross sections at the peak positions. We also note that, in the C-type-1 wave function, four nucleons forming an  $\alpha$  cluster just around  $^{44}\text{Ca}$  contain the components of the  $f$  and  $p$  orbits; however, it does not reproduce the cross section data.

What regions of the density profiles are actually observed? To answer this question, it is intuitive to look at the radial dependence of the scattering amplitude, i.e., integrand of the second term of Eq. (8) at a specific scattering angle [29], which is explicitly written as

$$g(\theta, b) = ikb e^{-2ikb \sin(\frac{\theta}{2}) + 2i\eta \ln(kb)} (1 - e^{i\chi_{sT}(b)}). \quad (13)$$

It is worthwhile to recall the relation

$$f(\theta) = F_C(\theta) + \int_0^\infty db g(\theta, b). \quad (14)$$

We set  $\theta$  near the first and second diffraction peaks and compare  $g$  with the different AQCM configurations as a function of the impact parameter  $b$ . Here we take the S-type and C-type-3 configurations, where the most different results are expected.

Figure 4 displays the real and imaginary parts of  $g$  obtained with S-type and C-type-3 for the differential elastic scattering cross sections around (a) the first peak ( $\theta = 7.8^\circ$ ) and (c) the second peak ( $\theta = 13^\circ$ ) positions. To see the difference more clearly, we also plot the absolute difference of the real and imaginary parts of  $g$  between S-type and C-type-3 for (b) the first peak and (d) second peak positions. At the first peak position [Figs. 4(a) and 4(b)], the absolute difference in  $g$  is largest at the surface region  $b \approx 4$  fm, which is consistent with our basis that the nuclear diffuseness is most reflected in the first diffraction peak [29], considering that the range of the nucleon-nucleon interaction is about 1 fm. At the second peak position [Figs. 4(c) and 4(d)], the difference is also largest at the surface region. The second peak region includes the information of the density wider than the surface region, and there the picture of the  $jj$ -coupling shell model works well. Here, the contribution around the tail region ( $b \approx 6$  fm) in Fig. 4(d) is reduced from that in Fig. 4(b) compared to the reduction of the surface region ( $b \approx 4$  fm), and thus, the

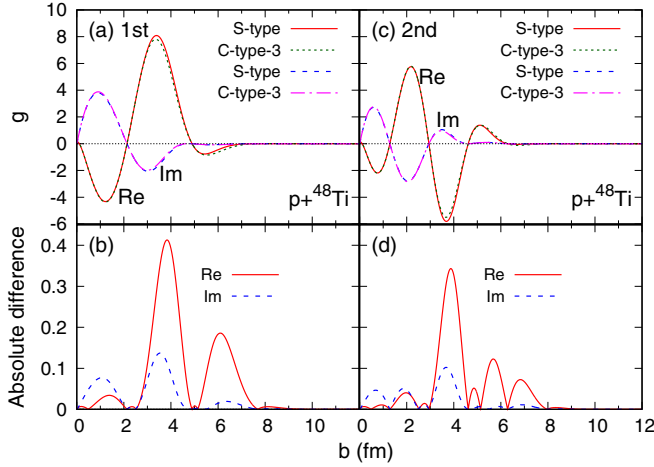


FIG. 4. Real and imaginary parts of the radial scattering amplitudes [Eq. (13)] around the (a) first and (c) second diffraction peaks of S-type and C-type-3, and their absolute differences of the two configurations for the (b) first and (d) second peak positions for proton- $^{48}\text{Ti}$  scattering. See text for details. The incident proton energy is chosen as 1000 MeV.

second peak reflects the difference of S-type and C-type-3 around the surface region more pronouncedly than the first peak.

From the analysis of the proton-nucleus elastic scattering, we have found that the  $^{48}\text{Ti}$  nucleus has a  $jj$ -coupling shell model structure rather than the  $\alpha + ^{44}\text{Ca}$  cluster structure. However, as discussed earlier, the  $\alpha$  knockout reaction cross section, which is sensitive to the tail region of the wave function, is explained by the  $\alpha + ^{44}\text{Ca}$  cluster structure with a large relative distance.

Indeed, we can deduce the vestige of the  $\alpha$  clustering in the tail region of the wave function from the  $\alpha$ -nucleus elastic scattering cross section. Figure 5 shows the differential cross section of the  $\alpha$  scattering on  $^{48}\text{Ti}$  at 240 MeV. Here, (a) and (b) show the results in the logarithmic and linear scales, respectively. The results of S-type, C-type-1, and C-type-2 are almost identical despite that the C-type configurations have more diffused nuclear surface than that of S-type. As can be recognized in Fig. 5(b), the density of C-type-3 best reproduces the experimental data [41].

Figure 6 draws (a) the real and imaginary parts of  $g$  of S-type and C-type-3 around the first peak position of the  $\alpha$ - $^{48}\text{Ti}$  elastic scattering cross sections ( $\theta = 7.2^\circ$ ) and (b) the absolute difference in the  $g$  values obtained with these configurations. No difference appears at  $b \lesssim 4$  fm because the  $\alpha$ -nucleus scattering is strongly absorptive. The difference is peaked at  $b \approx 5$  fm, which corresponds to the sum of the matter radii of  $\alpha$  and  $^{48}\text{Ti}$ . The  $\alpha$ -nucleus scattering has no sensitivity to the inner region and is only sensitive to the outer region of the nuclear density, while the proton-nucleus scattering probes the density profile near the nuclear surface. Thus, it could be interpreted that while the surface region of  $^{48}\text{Ti}$  is explained by the  $jj$ -coupling shell model configuration, the tail region is better explained by the  $\alpha$  clustering configuration. This result suggests the possibility of a change

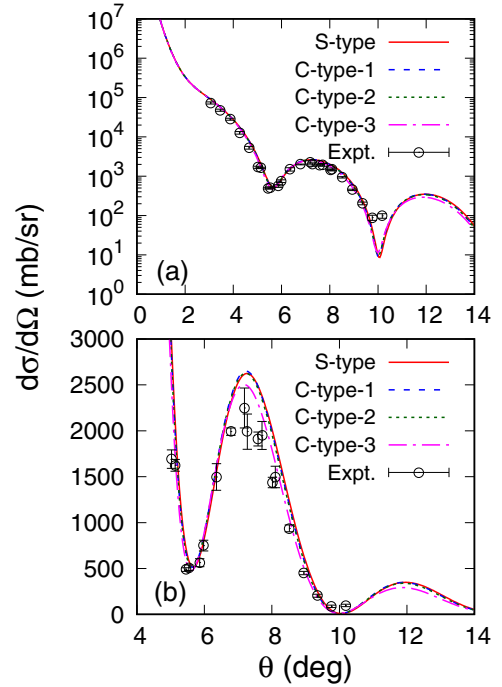


FIG. 5. Differential cross sections for the  $\alpha + ^{48}\text{Ti}$  elastic scattering at the incident  $\alpha$  particle energy of 240 MeV in logarithmic (a) and linear (b) scales as a function of the scattering angle. The experimental data are taken from Ref. [41].

in structure as a function of the distance from the center, from the  $jj$ -coupling shell model to the cluster model. We remark that a similar phenomenon has been discussed in  $^{44}\text{Ti}$ , where the  $\alpha$  cluster structure is completely broken in the region at small  $\alpha$ - $^{40}\text{Ca}$  distances due to the strong spin-orbit contribution. However, with increasing relative distances, the  $\alpha$  cluster structure appears beyond the interaction range of the

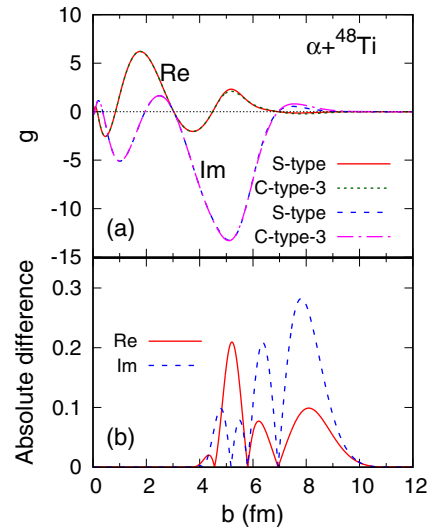


FIG. 6. Same as Fig. 4 but around the first peak position of the  $\alpha + ^{48}\text{Ti}$  elastic scattering cross section at the incident  $\alpha$  particle energy of 240 MeV.

spin-orbit interaction from the  $^{40}\text{Ca}$  nucleus. Here, the tensor interaction plays a crucial role in the  $\alpha$  clustering [42].

#### IV. CONCLUSION

The  $\alpha$  clustering in medium-mass nuclear systems is currently a topic of much discussion, and recent analysis of the  $\alpha$  knockout reaction on  $^{48}\text{Ti}$  has raised questions about whether  $^{48}\text{Ti}$  is shell-like or cluster-like. To address this issue, this study was conducted that involves calculating the proton- and  $\alpha$ - $^{48}\text{Ti}$  elastic scattering. Four types of density distributions were generated, including the  $jj$ -coupling shell model and three cluster model configurations, fully microscopically with AQCМ. The Glauber model was used to obtain these cross sections. We found that the  $jj$ -coupling shell model configuration best reproduces the experimental value of the high-energy proton-nucleus elastic scattering cross sections at the first and second diffraction peaks, which are sensitive to the surface region of the wave function.

On the other hand, a comparison of theoretical and experimental cross sections of the  $\alpha$ -nucleus elastic scattering clarifies the importance of the  $\alpha$  clustering in the tail region.

These results suggest that the structure of the nucleus changes as a function of the distance from the center. The  $jj$ -coupling shell model structure dominates the surface region of the nuclear system, but the structure changes to an  $\alpha+^{44}\text{Ca}$  cluster structure in the tail region, in agreement with the analysis of the  $\alpha$  knockout reaction.

The study shows that although the  $jj$ -coupling shell model wave function dominates around the surface region of  $^{48}\text{Ti}$ ,  $\alpha$  clustering is important in the tail region of the wave function. Understanding such a structural change in the tail region could provide an explanation for the clustering beyond medium-mass nuclei, leading to a more comprehensive understanding of  $\alpha$  decay. Traditional shell and mean-field models significantly underestimate the  $\alpha$  decay probabilities of heavy nuclei, which could be improved by incorporating the current mechanism.

#### ACKNOWLEDGMENTS

This work was in part supported by JSPS KAKENHI Grants No. 18K03635, No. 22H01214, and No. 22K03618.

- 
- [1] M. G. Mayer and H. G. Jensen, *Elementary Theory of Nuclear Shell Structure* (John Wiley and Sons, New York, 1955).
- [2] F. Michel, G. Reidemeister, and S. Ohkubo, *Phys. Rev. Lett.* **57**, 1215 (1986).
- [3] T. Yamaya, S. Oh-ami, M. Fujiwara, T. Itahashi, K. Katori, M. Tosaki, S. Kato, S. Hatori, and S. Ohkubo, *Phys. Rev. C* **42**, 1935 (1990).
- [4] T. Yamaya, K. Katori, M. Fujiwara, S. Kato, and S. Ohkubo, *Prog. Theor. Phys. Suppl.* **132**, 73 (1998).
- [5] S. Bailey, T. Kokalova, M. Freer, C. Wheldon, R. Smith, J. Walshe, N. Curtis, N. Soić, L. Prepolec, V. Tokić *et al.*, *Phys. Rev. C* **100**, 051302(R) (2019).
- [6] Y. Taniguchi, K. Yoshida, Y. Chiba, Y. Kanada-En'yo, M. Kimura, and K. Ogata, *Phys. Rev. C* **103**, L031305 (2021).
- [7] N. Itagaki, H. Masui, M. Ito, and S. Aoyama, *Phys. Rev. C* **71**, 064307 (2005).
- [8] H. Masui and N. Itagaki, *Phys. Rev. C* **75**, 054309 (2007).
- [9] T. Yoshida, N. Itagaki, and T. Otsuka, *Phys. Rev. C* **79**, 034308 (2009).
- [10] N. Itagaki, J. Cseh, and M. Płoszajczak, *Phys. Rev. C* **83**, 014302 (2011).
- [11] T. Suhara, N. Itagaki, J. Cseh, and M. Płoszajczak, *Phys. Rev. C* **87**, 054334 (2013).
- [12] N. Itagaki, H. Matsuno, and T. Suhara, *Prog. Theor. Exp. Phys.* **2016**, 093D01.
- [13] H. Matsuno, N. Itagaki, T. Ichikawa, Y. Yoshida, and Y. Kanada-En'yo, *Prog. Theor. Exp. Phys.* **2017**, 063D01.
- [14] H. Matsuno and N. Itagaki, *Prog. Theor. Exp. Phys.* **2017**, 123D05.
- [15] N. Itagaki, *Phys. Rev. C* **94**, 064324 (2016).
- [16] N. Itagaki and A. Tohsaki, *Phys. Rev. C* **97**, 014307 (2018).
- [17] N. Itagaki, H. Matsuno, and A. Tohsaki, *Phys. Rev. C* **98**, 044306 (2018).
- [18] N. Itagaki, A. V. Afanasjev, and D. Ray, *Phys. Rev. C* **101**, 034304 (2020).
- [19] N. Itagaki, T. Fukui, J. Tanaka, and Y. Kikuchi, *Phys. Rev. C* **102**, 024332 (2020).
- [20] N. Itagaki and T. Naito, *Phys. Rev. C* **103**, 044303 (2021).
- [21] W. Horiuchi and N. Itagaki, *Phys. Rev. C* **106**, 044330 (2022).
- [22] W. Horiuchi and N. Itagaki, *Phys. Rev. C* **107**, L021304 (2023).
- [23] Y. Yamaguchi, W. Horiuchi, and N. Itagaki, *Phys. Rev. C* **108**, 014322 (2023).
- [24] D. M. Brink, Many-body description of nuclear structure and reactions, in *Proceedings of the International School of Physics Enrico Fermi, Course XXXVI*, edited by L. Bloch (Academic, New York, 1966), p. 247.
- [25] W. Horiuchi, Y. Suzuki, B. Abu-Ibrahim, and A. Kohama, *Phys. Rev. C* **75**, 044607 (2007); **76**, 039903(E) (2007).
- [26] W. Horiuchi, T. Inakura, T. Nakatsukasa, and Y. Suzuki, *Phys. Rev. C* **86**, 024614 (2012).
- [27] S. Terashima, H. Sakaguchi, H. Takeda, T. Ishikawa, M. Itoh, T. Kawabata, T. Murakami, M. Uchida, Y. Yasuda, M. Yosoi *et al.*, *Phys. Rev. C* **77**, 024317 (2008).
- [28] J. Zenihiro, H. Sakaguchi, T. Murakami, M. Yosoi, Y. Yasuda, S. Terashima, Y. Iwao, H. Takeda, M. Itoh, H. P. Yoshida, and M. Uchida, *Phys. Rev. C* **82**, 044611 (2010).
- [29] S. Hatakeyama, W. Horiuchi, and A. Kohama, *Phys. Rev. C* **97**, 054607 (2018).
- [30] R. J. Glauber, in *Lectures in Theoretical Physics*, edited by W. E. Brittin and L. G. Dunham (Interscience, New York, 1959), Vol. 1, p. 315.
- [31] Y. Suzuki, R. G. Lovas, K. Yabana, and K. Varga, *Structure and Reactions of Light Exotic Nuclei* (Taylor & Francis, London, 2003).
- [32] B. Abu-Ibrahim, W. Horiuchi, A. Kohama, and Y. Suzuki, *Phys. Rev. C* **77**, 034607 (2008); **80**, 029903(E) (2009); **81**, 019901(E) (2010).
- [33] W. Horiuchi, S. Hatakeyama, S. Ebata, and Y. Suzuki, *Phys. Rev. C* **93**, 044611 (2016).

- [34] S. Hatakeyama and W. Horiuchi, *Nucl. Phys. A* **985**, 20 (2019).
- [35] K. Varga, S. C. Pieper, Y. Suzuki, and R. B. Wiringa, *Phys. Rev. C* **66**, 034611 (2002).
- [36] B. Abu-Ibrahim, S. Iwasaki, W. Horiuchi, A. Kohama, and Y. Suzuki, *J. Phys. Soc. Jpn.* **78**, 044201 (2009).
- [37] T. Nagahisa and W. Horiuchi, *Phys. Rev. C* **97**, 054614 (2018).
- [38] I. Angeli and K. P. Marinova, *At. Data Nucl. Data Tables* **99**, 69 (2013).
- [39] G. D. Alkhozov, T. Bauer, R. Beurtey, A. Boudard, G. Bruge, A. Chaumeaux, P. Couvert, G. Cvijanovich, H. H. Duham, J. M. Fontaine *et al.*, *Nucl. Phys. A* **274**, 443 (1976).
- [40] W. Horiuchi, *Prog. Theor. Exp. Phys.* **2021**, 123D01.
- [41] Y. Tokimoto, Y.-W. Lui, H. L. Clark, B. John, X. Chen, and D. H. Youngblood, *Phys. Rev. C* **74**, 044308 (2006).
- [42] C. Ishizuka, H. Takemoto, Y. Chiba, A. Ono, and N. Itagaki, *Phys. Rev. C* **105**, 064314 (2022).